

Cite this: *Nanoscale*, 2021, **13**, 20225

# Synergistic roles of vapor- and liquid-phase epitaxy in the seed-mediated synthesis of substrate-based noble metal nanostructures†

 Spencer D. Golze,<sup>‡a</sup> Robert A. Hughes,<sup>‡a</sup> Eredzhep Menumorov,<sup>a</sup> Sergei Rouvimov<sup>b</sup> and Svetlana Neretina <sup>\*a,c</sup>

Colloidal growth modes reliant on the replication of the crystalline character of a preexisting seed through homoepitaxial or heteroepitaxial depositions have enriched both the architectural diversity and functionality of noble metal nanostructures. Equivalent syntheses, when practiced on seeds formed on a crystalline substrate, must reconcile with the fact that the substrate enters the syntheses as a chemically distinct bulk-scale component that has the potential to impose its own epitaxial influences. Herein, we provide an understanding of the formation of epitaxial interfaces within the context of a hybrid growth mode that sees substrate-based seeds fabricated at high temperatures in the vapor phase on single-crystal oxide substrates and then exposed to a low-temperature liquid-phase synthesis yielding highly faceted nanostructures with a single-crystal character. Using two representative syntheses in which gold nanoplates and silver–platinum core–shell structures are formed, it is shown that the hybrid system behaves unconventionally in terms of epitaxy in that the substrate imposes an epitaxial relationship on the seed but remains relatively inactive as the metal seed imposes an epitaxial relationship on the growing nanostructure. With epitaxy transduced from substrate to seed to nanostructure through what is, in essence, a relay system, all of the nanostructures formed in a given synthesis end up with the same crystallographic orientation relative to the underlying substrate. This work advances the use of substrate-induced epitaxy as a synthetic control in the fabrication of on-chip devices reliant on the collective response of identically aligned nanostructures.

 Received 22nd October 2021,  
Accepted 27th November 2021  
DOI: 10.1039/d1nr07019c

[rsc.li/nanoscale](http://rsc.li/nanoscale)

## 1. Introduction

Epitaxy is one of the foundational concepts in materials preparation. Its importance stems from the ability of atoms arriving at a surface to form organized arrangements that replicate the surface atomic structure of a crystalline substrate. Broadly categorized into homoepitaxy and heteroepitaxy depending on whether or not the depositing material is identical to the substrate, such epitaxial relationships can lock in a specific crystallographic orientation and lead to the formation of a coherent interface between dissimilar materials. When depositions

are carried out under kinetically favorable conditions, epitaxial growth can occur *via* the Frank–van der Merwe, Volmer–Weber, or Stranski–Krastanov growth modes where these classifications depend upon whether the growth proceeds in a layer-by-layer manner, as discrete islands followed by coalescence, or in a layer-by-layer manner up to a critical thickness followed by island growth. Crystal lattice misfit strain is a crucial parameter in determining which mode takes hold as well as the degree to which lattice imperfections such as stacking faults, twins, dislocations, and bending are introduced as a means to partially relax a strained material. With such epitaxial techniques proving transformative to semiconductor thin film technologies, it is not surprising that these same concepts, when applied to nano-based syntheses, yield nanostructures with diverse architectures and a rich set of technologically relevant phenomena.<sup>1–5</sup>

Recognizing the nature of the metal/metal interface as being integral to the synthesis of core–shell nanostructures, Habas *et al.*<sup>6</sup> carried out the first study that singled out the heteroepitaxial relationship formed between two metals as being a key parameter in shaping bimetallic colloidal nano-

<sup>a</sup>College of Engineering, University of Notre Dame, Notre Dame, Indiana, 46556, USA. E-mail: [sneretina@nd.edu](mailto:sneretina@nd.edu)

<sup>b</sup>Notre Dame Integrated Imaging Facility (NDIIF), University of Notre Dame, Notre Dame, Indiana, 46556, USA

<sup>c</sup>Department of Chemistry and Biochemistry, University of Notre Dame, Notre Dame, Indiana, 46556, USA

†Electronic supplementary information (ESI) available. See DOI: 10.1039/d1nr07019c

‡Equal Contribution.

crystals.<sup>7</sup> They demonstrated that, while the coherent heteroepitaxial relationship formed at the Pt/Pd interface allows for a conformal growth mode and the emergence of highly faceted Pt@Pd core-shell structures, a Au/Pt interface gives rise to the formation of twin defects that seed the growth of pentagonally twinned Au nanorods. With Pt/Pd and Pt/Au interfaces having a lattice-mismatch of 0.77% and 4.08%, respectively, the authors concluded that lattice-matched heteroepitaxial interfaces are more amenable to the formation of core-shell structures. Although numerous studies have demonstrated the validity of their conclusions, there are now notable exceptions where lattice-matched systems give rise to asymmetric growth modes<sup>8,9</sup> and where lattice mismatches in excess of 7% result in highly symmetric core-shell structures exhibiting sharp interfaces.<sup>10–13</sup> More significant, however, is that a great many studies have now demonstrated a remarkable set of properties that have their origins in nanostructure heteroepitaxy. With its influences now deemed responsible for (i) strain-induced catalytic activity,<sup>14–18</sup> (ii) enhancements to magnetic coercivity,<sup>19–21</sup> (iii) conformal,<sup>6,22–24</sup> asymmetric,<sup>4,6,11,25,26</sup> dendritic,<sup>23,27</sup> polymorphic,<sup>28–30</sup> and pseudomorphic<sup>31</sup> growth modes, (iv) enhanced thermal<sup>32</sup> and chemical stability,<sup>33–35</sup> (v) the formation of twin defects,<sup>6,36</sup> dislocations,<sup>25,31,37,38</sup> stacking faults,<sup>38</sup> and surface reconstructions,<sup>32</sup> and (vi) the restructuring of nanostructures in response to a changing chemical environment,<sup>39,40</sup> epitaxy has been unequivocally demonstrated as essential to the design and understanding of bimetallic nanocrystals.

Substrate-based single-crystal noble metal nanostructures are increasingly being recognized as a highly desirable platform for on-chip applications in chemical and biological sensing, nanoelectronics, and metamaterials.<sup>41–44</sup> Such structures bring a distinct set of physicochemical properties to the substrate surface by allowing for nanostructure architectures that are not readily obtainable through lithographic processes. Within this realm there is the opportunity to use the epitaxial relationship between the nanostructure and a crystalline substrate as a synthetic control that is able to dictate the alignment of the nanostructure relative to the substrate surface. It is, however, exceedingly difficult to use colloidal methods to spontaneously nucleate epitaxially aligned metal nanostructures on the most commonly used substrate materials. Syntheses carried out in the vapor phase have proved far more viable as numerous examples exist where nanostructure formation is guided by the heteroepitaxial relationship formed with planar crystalline substrates.<sup>45–51</sup> Such syntheses, however, typically require processing temperatures far in excess of those used to generate nanostructures in liquid media if single-crystal structures are to be obtained and where the influences of substrate surface reconstructions are to be avoided or, at least, controlled.<sup>48,50,51</sup> Moreover, shape control is rather limited because high temperatures tend to promote low surface energy morphologies and the rounding of corners, although notable exceptions do occur.<sup>45–47</sup>

A hybrid strategy, which allows for both epitaxy and nanostructure shape control, uses vapor-phase assembly processes

to form roundish single-crystal nanostructures having a heteroepitaxial relationship with a crystalline substrate that then act as seeds for syntheses carried out in liquid media.<sup>52</sup> In doing so, homoepitaxial<sup>53,54</sup> and heteroepitaxial<sup>55,56</sup> depositions onto these substrate-based seeds can proceed in much the same manner as they do in seed-mediated colloidal syntheses. They differ from colloidal syntheses in that nanostructure growth requires that it occur not just on the seed but where the nanostructure growth front encounters the substrate to form an interface. From the standpoint of epitaxy, such nanostructures are intriguing in that the seed and nanostructure are formed under vastly different conditions, and where for core-shell structures, misfit strains of different signs and magnitude can occur at the core/shell, core/substrate, and shell/substrate interfaces. Herein, we report on the interfacial control mechanisms for nanostructures synthesized using this hybrid strategy for the case where substrate-imposed epitaxy ultimately dictates both the in-plane and out-of-plane alignment of the nanostructure. In advancing this understanding, two previously studied syntheses<sup>54,55</sup> act as model systems that differ in that one sees metal-on-metal growth that is homoepitaxial while the other is heteroepitaxial. This work forwards the use of epitaxy as a synthetic control in the rational design of photo- and chemically-active surfaces reliant on substrate-based single-crystal nanostructures.

## 2. Results

### 2.1 Two-component system

A two-component Au-sapphire system was examined in which Au seeds are formed on a [0001]-oriented sapphire (*i.e.*, Al<sub>2</sub>O<sub>3</sub>) substrate, after which Au<sup>3+</sup> ions are reduced onto the seeds in a liquid-state chemical environment amenable to nanoplate synthesis (Fig. 1a). From an epitaxial standpoint, a Au/sapphire interface seems like an unlikely candidate for realizing a heteroepitaxial relationship since a union must be formed between the face-centered cubic (fcc) crystal structure of Au and the hexagonal crystal structure of sapphire. This symmetry mismatch is, however, accommodated by the (111) planes of Au since they express a two-dimensional hexagonal symmetry due to the hexagonal close-packed arrangement of atoms within these planes (Fig. 1b). Nevertheless, the combination still has a high lattice mismatch since the center-to-center distance between Au atoms of 2.884 Å is incommensurate with the 4.758 Å *a*-axis of sapphire. The best-case alignment scenario (Fig. 1b) leads to a lattice mismatch of 5.0% where Au is strained compressively. The seed-mediated liquid-state nature of the nanoplate synthesis further adds to the intrigue of the resulting epitaxial relationship since the emergence of a planar geometry necessitates the formation of a large-area interface with a lattice-mismatched substrate.

Fig. 1c–e shows scanning electron microscopy (SEM) images of a Au seed array and the nanoplates that emerge from a light-mediated liquid-state synthesis that is described in detail elsewhere.<sup>54</sup> The seeds are unique in that they have a

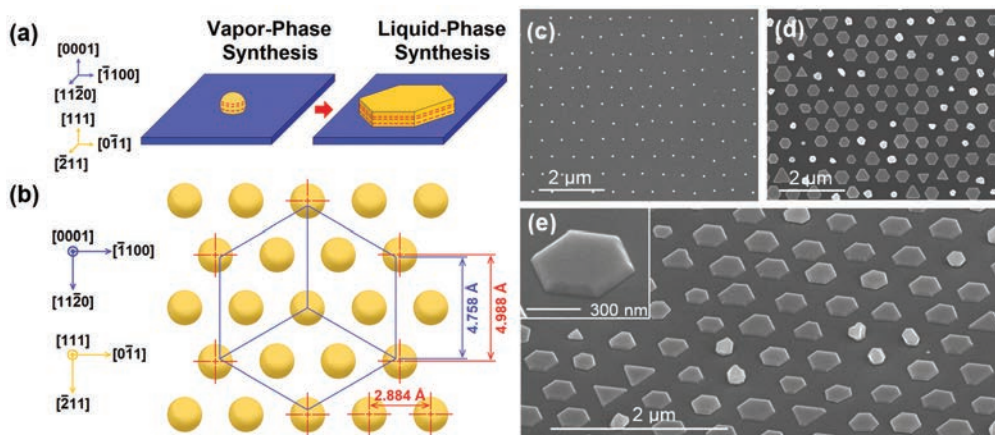


**Fig. 1** Schematics showing (a) the architectural transformation that a Au seed undergoes during a room temperature liquid-phase synthesis where the red dashed lines denote the protrusion of stacking fault defects from the Au surface and (b) the crystallographic alignment of Au atoms (yellow) in their (111) plane relative to the hexagonal unit cell dimensions of sapphire (blue). Top view SEM images of a Au (c) seed and (d) nanoplate array. (e) Tilted view image where the inset shows a single nanoplate.

single-crystal character but where stacking fault defects occur along the [111] direction normal to the substrate surface. Such defects, which are likely induced by substrate-imposed strains,<sup>54</sup> are essential to the nanoplate growth mode since they provide a symmetry-breaking structure with a two-dimensional character in an otherwise isotropic metal.<sup>42</sup> Also of significance is that seed fabrication requires temperatures as high as 1010 °C if nanoplates are to be obtained in high yield. The liquid-state nanoplate synthesis, in stark contrast to seed fabrication, is carried out at room temperature. The synthesis, which occurs in a solution of HAuCl<sub>4</sub>, PVP, methanol, and H<sub>2</sub>O, supports a two-dimensional growth mode because Au is preferentially reduced on the seed edges where the planar stacking faults protrude. The growth mode, hence, requires not only the homoepitaxial deposition of Au onto the seed but must also replicate the defect structure if the growth mode is to persist. Fig. S1 of the ESI† shows the existence of stacking faults and demonstrates that they do, in fact, extend from one side of the seed to the other. A striking feature of the arrayed surfaces is that all of the hexagonal nanoplates are identically oriented relative to the substrate surface, an outcome that provides incontrovertible evidence that each nanoplate shares the same heteroepitaxial relationship with the sapphire substrate. The nonplanar Au structures with irregular shapes that appear at some of the array positions are a product of seeds that are defective in that they lack the internal defect structure needed to promote a planar growth mode.<sup>54</sup>

With vastly different synthesis temperatures (*i.e.*, 1010 *versus* 23 °C), the seed/substrate and nanoplate/substrate interfaces were examined separately. Fig. 2a shows a transmission electron microscopy (TEM) cross section of five seeds prepared using focused ion beam (FIB) techniques. Even at these low magnifications, a difference in contrast is clearly visible below each seed. The seeds themselves appear roundish but where weak faceting is apparent. Fig. 2b shows a high-resolution TEM (HRTEM) image of the Au seed/sapphire interface and

corresponding selected area electron diffraction (SAED) images. The data confirms the anticipated 0.24 and 0.22 nm *d*-spacings for (111) Au and (0006) sapphire planes, respectively. The SAED patterns are consistent with those expected for  $[\bar{2}11]$  Au and  $[11\bar{2}0]$  sapphire zone axes. The overall crystallographic relationship for this seed/substrate interface is, hence, given by  $(111)[\bar{2}11]_{\text{Au}} || (0001)[11\bar{2}0]_{\text{sapphire}}$ , a result consistent with X-ray diffraction data derived from pole figure analysis.<sup>57</sup> The interface appears highly ordered, although somewhat distorted. Also revealing is the low-resolution TEM image of the entire seed because it shows that the substrate directly below it is somewhat elevated when compared to the adjacent area. A similar substrate surface reconstruction has been observed for a Au/MgAl<sub>2</sub>O<sub>4</sub> interface,<sup>51</sup> albeit one that is far more exaggerated than that shown here.

Fig. 2c shows an image of a FIB cross section for a Au nanoplate cut across its center point. The Au/sapphire interface displayed shows a narrow interfacial layer that runs the length of the nanoplate except for small region near its center (denoted by the green circle) where the seed is expected to reside. Also noteworthy is that this layer extends beyond the perimeter of the nanoplate. Fig. 2d shows a representative HRTEM image of the nanoplate/substrate interface for an area where the liquid-state Au nanoplate growth mode was active (denoted by the red box in Fig. 2c) and SAED patterns corresponding to areas occupied by (i) just the Au nanoplate, (ii) the interface, and (iii) just the sapphire substrate. The interface associated with the liquid-state growth mode appears more disordered than the equivalent interface formed in the vapor state (Fig. 2b) but where there still exists sufficient crystallinity within the selected area to obtain a diffraction pattern. Despite this interfacial disorder, the Au nanoplate SAED pattern away from the interface shows an ordering along its  $[\bar{2}11]$  zone axis that is essentially identical to that displayed by the seed. The implication of this result is that the liquid-state Au nanoplate growth mode is little affected by the interfacial disorder. It

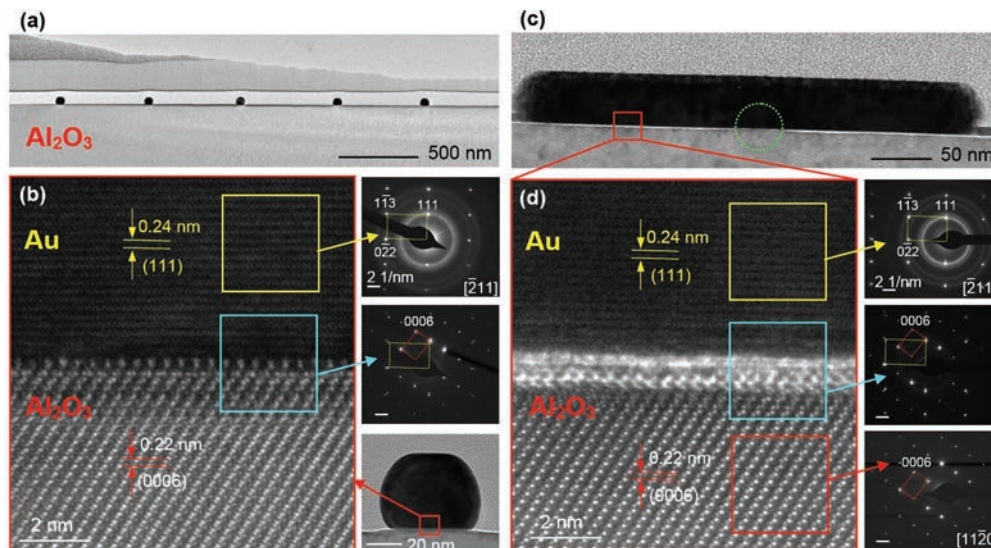


**Fig. 2** (a) TEM image of Au seeds on a [0001]-oriented sapphire (*i.e.*,  $\text{Al}_2\text{O}_3$ ) substrate after FIB cross-sectioning. (b) HRTEM image of an ordered seed/substrate interface with corresponding SAED patterns. (c) Cross-sectional TEM image of a single Au nanoplate. (d) HRTEM image of a disordered nanoplate/substrate interface with corresponding SAED patterns.

should also be noted that the bonding that occurs at the nanoplate/substrate interface is sufficiently strong to endure sonication.<sup>57</sup>

The nanoplate growth mode is one that is well-studied when occurring as a colloid. It requires crystalline seeds with stacking fault defects whereby  $\text{Au}^{3+}$  ions are selectively reduced onto surfaces where the stacking faults protrude while capping agents prevent the nanoplates from thickening much beyond the initial seed diameter.<sup>58,59</sup> From the standpoint of homoepitaxy, this growth mode is fascinating in that depositing atoms must exactly replicate the surface atomic structure of the seed such that both the existing crystallinity and stacking fault defects remain intact. When practicing a nanoplate synthesis on substrate-based seeds, the main features of this colloidal growth mode are preserved<sup>54,57</sup> despite the presence of a lattice-mismatched substrate. The results presented here show that Au nanoplate growth is accompanied by the formation of a thin interfacial layer at the substrate surface as no such layer exists prior to its insertion in the nanoplate growth solution. The layer, which is likely a result of an interaction between sapphire and the aqueous environment in which the nanoplates are synthesized,<sup>60</sup> negates the possibility of forming a crisp Au nanoplate/sapphire interface. Yet this seemingly detrimental interfacial layer does not prove disruptive to nanoplate growth. The results are consistent with an overall growth mode in which Au-sapphire epitaxy is only active during the vapor-phase seed formation process, after which the substrate plays a relatively passive role in the evolution of the nanoplate. With Au-on-Au homoepitaxy proceeding on the nanoplate edge in a layer-by-layer manner from nucleation events occurring where the stacking fault defects protrude, the Au/sapphire interface is only formed as each layer intersects the substrate. This inevitably minimizes the extent to which sapphire interfacial dis-

order can disrupt the growth mode. In such a scenario, it is the unconventional nature of the liquid-phase growth mode that allows for homoepitaxial growth off the seed surface while largely negating disruptions caused by a disordered interface.

## 2.2 Three-component system

A three-component Pt-Ag-LSAT (*i.e.*,  $\text{La}_{0.18}\text{Sr}_{0.82}\text{Al}_{0.59}\text{Ta}_{0.41}\text{O}_3$ ) system was examined in which Pt nanostructures are formed on a [100]-oriented LSAT substrate after which  $\text{Ag}^+$  ions are reduced onto the Pt surface to form a Pt@Ag core-shell structure. The system combines three cubic materials with lattice constants of 3.924, 4.085, and 3.868 Å for Pt, Ag, and LSAT, respectively. As such, the Pt/LSAT, Ag/Pt, and Ag/LSAT interfaces have lattice mismatches of 1.45%, 4.10%, and 5.61%, respectively. Thus, when Pt is formed on the substrate, it is subject to only a slight compressive strain due to an excellent lattice match. This, however, is not the case for the Ag shell as an epitaxial interface requires that it cope with compressive strains at interfaces formed with both the Pt core and LSAT substrate.

The Pt@Ag core-shell structures were formed using procedures that are described in detail elsewhere<sup>55</sup> but where in the current work (100)-oriented LSAT is used as the substrate material instead of [0001]-oriented sapphire. The synthesis, which is shown schematically in Fig. 3a, begins with the sequential deposition of Sb, Bi, and Pt films followed by a heating regimen that sees the triple-layer heated to 1100 °C such that roundish Pt nanoparticles are formed (see ESI, Fig. S4†). This vapor-phase assembly process shares many similarities with solid-state dewetting<sup>61</sup> but where the inclusion and subsequent evaporation of the sacrificial Bi/Sb layers is advantageous in that it enhances the dewetting process<sup>62</sup> such that single-crystal Pt nanostructures are formed

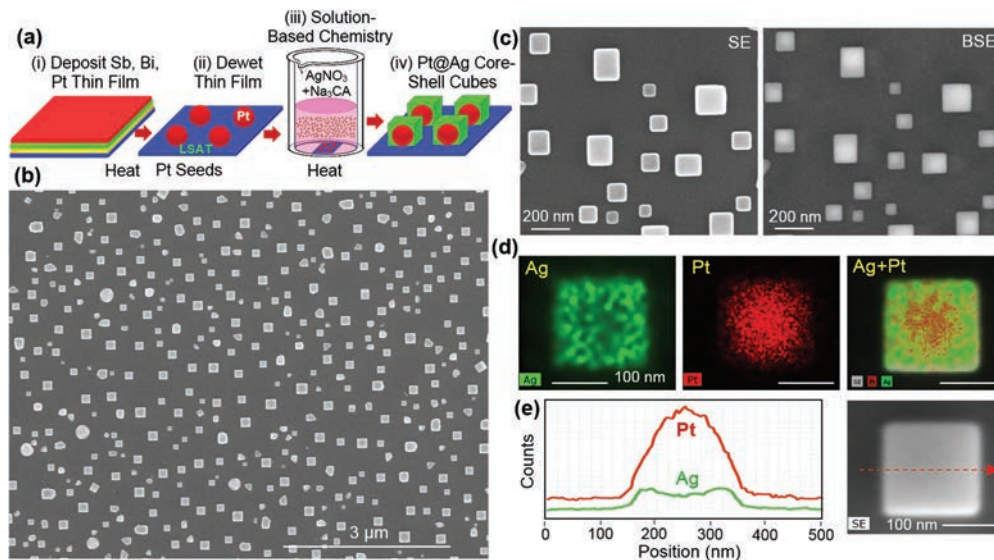


**Fig. 3** (a) Schematic of the processing route used to form substrate-based Pt@Ag nanocubes whereby Pt nanostructures are formed in the vapor phase followed by a liquid-state synthesis that sees  $\text{Ag}^+$  reduced onto their surface. (b) Top view SEM image of Pt@Ag nanocubes. (c) SEM images taken in SE and BSE modes. (d) EDS elemental mapping and (e) the associated line scans for Ag and Pt.

that express shape uniformity. When the dewetting of Pt films is performed without this layer, it leads to an unsatisfactory product with a large number of misshapen structures, many of which are bi-crystals.<sup>49</sup> Once formed, the Pt nanostructures are subjected to a 95 °C three-reagent liquid-phase aqueous synthesis (*i.e.*,  $\text{AgNO}_3$ , trisodium citrate, nitric acid) that promotes the formation of heteroepitaxially deposited Ag shell with (100) facets. Fig. 3b shows an SEM image of the [100]-oriented Pt@Ag nanocubes formed where their epitaxial relationship with the substrate is made apparent by the alignment of nanocube facets. Some of the structures, however, express irregularly shaped geometries while others are elongated, appearing rectangular rather than square when viewed from above. Fig. 3c shows a magnified view of the same structures taken in secondary electron (SE) and backscattered electron (BSE) modes where the Z-contrast accessible in the BSE mode reveals that many of the cores are offset from the central position. Elemental mapping and the associated line scans (Fig. 3d and e) made possible using energy-dispersive spectroscopy (EDS) are consistent with a Pt@Ag core-shell geometry. It should be noted that this synthesis, while not the first to synthesize nanocubes with the [100]-axis normal to the substrate surface,<sup>27</sup> is unique because of the epitaxial alignment obtained. Moreover, by substituting [100]-oriented LSAT for [0001]-oriented sapphire it is possible to alter the epitaxial relationship between the Pt seed and the substrate such that the [111]-axis of the resulting nanocube is normal to the substrate surface (see ESI, Fig. S3†), a result that further demonstrates epitaxy as a viable synthetic control.

A TEM cross section was prepared using FIB techniques to examine the various interfaces within the structure (Fig. 4a). The image confirms the core-shell morphology as both the Ag and Pt components are readily resolved. It also captures two

structures that deviate from the nanocube geometry (denoted by yellow arrows) where in both cases it is the Ag deposition that is responsible for the deviation as the Pt cores appear quite similar for all six structures. Fig. 4b shows a HAADF-STEM image of a single Pt@Ag structure. It highlights one of the key differences between core-shell structures synthesized using substrate-based seeds and those formed as colloids in that the Ag shell is unable to fully encapsulate the Pt core because the substrate blocks access to its lower surface. This steric hindrance, as has been described previously,<sup>27,55,56</sup> inevitably leads to core-shell structures that are asymmetric. The image also reveals that the Pt core is multifaceted as has been observed in other high-temperature vapor-phase syntheses reliant on solid-state dewetting.<sup>49</sup> The Ag shell is well-faceted except for its rounded corners. The bimetallic nature of the core-shell structure is further supported by the EDS line scan taken through the center of the structure along a line normal to the substrate surface (Fig. 4c) in that it shows the anticipated profile.

Fig. 4d–f shows a HRTEM image of the Pt/LSAT, Ag/Pt, and Ag/LSAT interfaces, respectively. Although there exists a close lattice match between Pt and LSAT, the interface is not as pristine from a heteroepitaxial standpoint as it is for other materials that have a close lattice match with the LSAT substrate.<sup>63,64</sup> This is likely attributable to damage to the substrate surface incurred during the vapor-phase assembly of Pt nanostructures in which Bi and Sb are used as sacrificial materials. The Bi/Sb multilayer is used because Bi, by itself, leaves the substrate scarred but where the incorporation of Sb, to a large extent, mitigates this issue. Notwithstanding, the Pt/LSAT interface is of sufficient quality to promote the desired heteroepitaxial relationship. Consistent with this conclusion is the corresponding SAED pattern that shows excellent align-

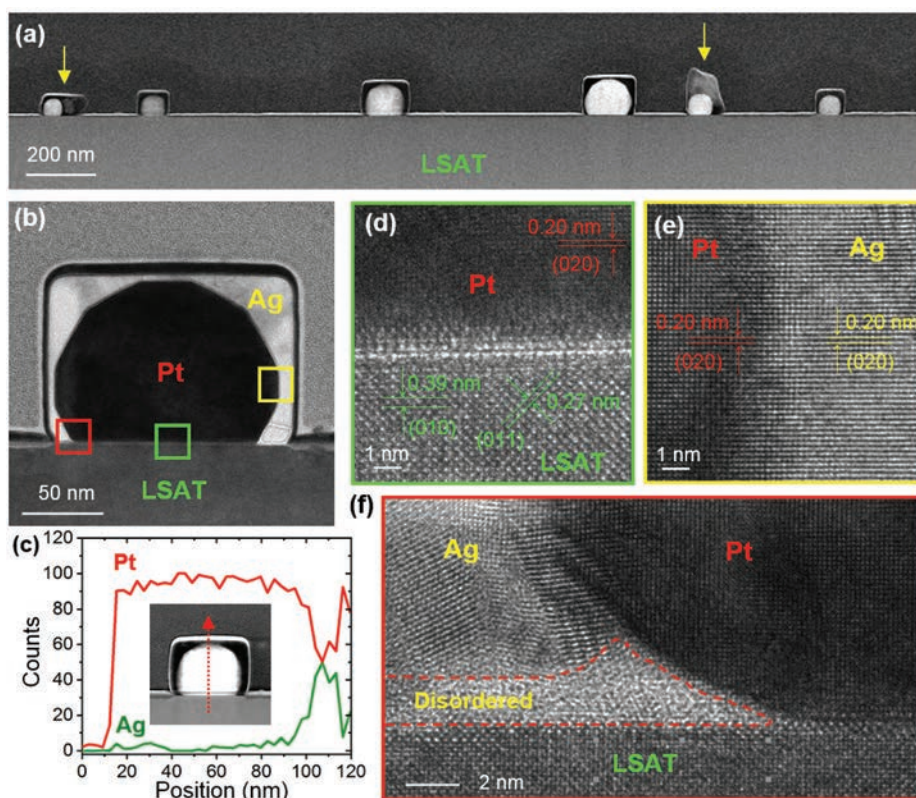


**Fig. 4** (a) HAADF-STEM image of Pt@Ag core-shell nanocubes on an LSAT substrate after FIB cross-sectioning. (b) Cross-sectional HAADF-STEM image of a single core-shell structure. (c) EDS line scans for Pt and Ag along the direction shown in the image. HRTEM images showing highly ordered (d) Pt/LSAT and (e) Ag/Pt epitaxial interfaces. (f) HRTEM image showing highly disordered Ag growth at Ag/LSAT interface. The green, yellow, and red boxes shown in Fig. 4b denote the positions where the three HRTEM images were taken.

ment of the Pt and LSAT diffraction spots when viewed along the [001] zone axis (see ESI, Fig. S4a†). The HRTEM image of the Ag/Pt interface reveals that a coherent interface has formed despite a lattice mismatch of 4.1% but where a slight splitting of diffraction spots is evident in the SAED pattern (see ESI, Fig. S4b†). The interface appears quite sharp where there exists no obvious evidence for interfacial alloying. In stark contrast, the Ag/LSAT interface appears highly disordered to the extent that it is even difficult to discern any particular crystallographic orientation. The result is, however, consistent with the two component Au-sapphire nanoplate system in that the metal/substrate interface formed in liquid media is of poor quality.

The core-shell growth mode brings together three chemically distinct components where all possible interface combinations are realized. The high-temperature assembly of Pt on LSAT through solid-state dewetting proves crucial in that the high temperatures used are able to promote an epitaxial relationship whereas the low-temperature liquid-state growth of Ag results in a Ag/LSAT interface that is disordered. Despite this interfacial disorder, the integrity of the Ag nanocube growth mode is maintained because the architecture and its orientation with respect to the substrate are guided by the heteroepitaxial relationship formed at the Ag/Pt interface during the liquid-phase synthesis. With some Pt@Ag core-shell struc-

tures showing asymmetric Ag growth around the Pt core, it is tempting to attribute their existence to growth mode disruptions caused by the substrate. Such offsets have, however, also been observed for colloidal core-shell nanostructures where their occurrence is attributed to some portion of the shell nucleating growth before others.<sup>10</sup> Nevertheless, it is important to note that the success of the Ag nanocube growth mode in achieving heteroepitaxially aligned Pt@Ag structures is not reliant on an epitaxial relationship being formed at the shell/substrate interface.

### 3. Discussion

The results presented herein, while investigating only two nanostructure-substrate combinations among a seemingly endless number of possibilities, provide key insights into the use of epitaxy as a synthetic control for generating aligned nanostructure architectures with a single-crystal character. In both instances, epitaxy proved possible for the high-temperature vapor-phase syntheses of metal nanostructures on single-crystal oxide substrates. The low-temperature liquid-phase synthesis, however, was able to promote epitaxial metal-on-metal depositions but, at the same time, was unable to realize an epi-

taxial relationship at the metal/oxide interface. These findings, by themselves, are not novel. Unique, however, is the interplay between the vapor- and liquid-phase growth modes in controlling both nanostructure alignment and architecture. By imposing an epitaxial relationship on the metal nanostructure formed in the vapor-phase synthesis and then remaining relatively passive in the liquid-state synthesis, the oxide substrate is still able to dictate the overall crystallographic alignment by using the heteroepitaxially aligned metal nanostructure formed in the vapor phase as a proxy for relaying crystallographic instructions to the liquid-state synthesis. Although such a growth pathway seems to add an unwanted degree of complication, it is advantageous in that a passive substrate during the liquid-phase synthesis (i) lessens the disruptive influence of substrate surface reconstructions or any processing- or synthesis-related surface damage, (ii) reduces heteroepitaxially-imposed strains that would otherwise be present at the nanostructure/substrate interface, (iii) increases the likelihood that colloidal growth modes will be adaptable to substrate-based seed-mediated syntheses, and (iv) potentially allows for the overgrowth or intersection with adjacent lithographically-defined structures.

The use of substrate-imposed epitaxy as a synthetic control provides the means to design photo- and chemically-active surfaces composed of identically oriented noble metal nanostructures. With this capability comes the opportunity to fabricate surfaces of plasmonic structures that exhibit a polarization-dependent response. Alignment also forwards the possibility of precisely designing surfaces with a high density of plasmonic nanogaps that are formed by having the sharp corners on adjacent structures grow toward each other. Although such capabilities are also being forwarded through assembly processes directed toward the precise placement of colloidal nanostructures on substrate surfaces,<sup>43,65–67</sup> the current approach provides advantages in that epitaxy allows for the formation of electrically-, optically-, and chemically-active interfaces that are unencumbered by intervening ligands and where the epitaxial connection can lead to strong adhesion. With the ability to adapt seed-mediated colloidal growth modes to syntheses carried out on substrate-supported seeds also comes the opportunity to advance the syntheses of substrate-based bimetallic nanostructures with designs that have already given rise to a remarkable set of properties and functionalities originating from metal-on-metal epitaxy.<sup>1–5</sup> With such capabilities of relevance to plasmonic sensing, metamaterials, and photocatalysis, the utilization of epitaxy in advancing on-chip functionalities could prove attractive. At the same time, there are disadvantages to the approach in that (i) the formation of an epitaxial relationship is by no means assured, (ii) forming single-crystal structures in the vapor phase on semiconducting substrates has proven difficult due to interdiffusion and the formation of low-temperature metal–semiconductor eutectics, and (iii) the vapor-phase assembly of small single-crystal seeds (<10 nm) can become challenging since twinned structures with icosahedral and decahedral morphologies become thermodynamically favored.<sup>68</sup>

## 4. Conclusion

In summary, we have examined the epitaxial constructs responsible for two representative hybrid growth modes that are able to realize substrate-based noble metal nanostructures expressing a high degree of alignment and shape uniformity. Taken together, they show the benefit in combining a high-temperature vapor-phase seed fabrication process with a low-temperature liquid-phase nanostructure synthesis in that metal–oxide epitaxy is achievable at high temperatures whereas low temperatures favor metal-on-metal epitaxy. Also crucial is that epitaxy can be transduced from substrate to seed to nanostructure where the formation of a metal–oxide interface in liquid-phase synthesis does not prove overly detrimental to the nanostructure growth mode. These findings, hence, enrich the design possibilities for photo- and chemically-active surfaces, and in doing so, forward the integration of single-crystal nanostructures into on-chip device platforms.

## 5. Experimental section

### 5.1 Materials

Targets used in the sputter deposition of Au (99.9985%) and Pt (99.99%) were fabricated from 0.5 mm thick foils (Alfa Aesar) using a punch and die setup. Disc-shaped Sb and Bi targets were sliced from rods with 99.999% purity (ESPI Metals). Sapphire ( $\text{Al}_2\text{O}_3$ ) and LSAT ( $\text{La}_{0.18}\text{Sr}_{0.82}\text{Al}_{0.59}\text{Ta}_{0.41}\text{O}_3$ ) substrates were sourced from MTI Corporation. Nanoimprint lithography utilized a Si stamp (Lightmyth Technologies), a 7030R thermal resist (Micro Resist Technology, GmbH), and a trichloro(1*H*,1*H*,2*H*,2*H*-perfluoro-octyl)silane antisticking layer (MilliporeSigma). Vapor-phase syntheses were carried out in ultrahigh purity argon (Airgas). The Au nanoplate synthesis utilized hydrogen tetrachloroaurate(III) trihydrate ( $\text{HAuCl}_4 \cdot 3\text{H}_2\text{O}$ , Alfa Aesar), polyvinylpyrrolidone (PVP, MW = 40 000, MilliporeSigma), methanol ( $\text{CH}_3\text{OH}$ , VWR), and deionized (DI) water derived from a Milli-Q system (18.2 M $\Omega$  cm at 25 °C). The Ag nanocube shell synthesis utilized 99.9999% silver nitrate ( $\text{AgNO}_3$ , MilliporeSigma), 99% trisodium citrate dihydrate ( $\text{Na}_3\text{C}_6\text{H}_5\text{O}_7 \cdot 2\text{H}_2\text{O}$ , Alfa Aesar), 99% L-ascorbic acid ( $\text{C}_6\text{H}_8\text{O}_6$ , Fisher Scientific), and nitric acid ( $\text{HNO}_3$ , MilliporeSigma).

### 5.2 Nanoplate synthesis

Au nanoplates were formed on [0001]-oriented sapphire substrates using a plasmon-mediated synthesis described in detail elsewhere.<sup>54</sup> The procedure begins by defining a Au seed array using nanoimprint lithography (NIL) in combination with a high-temperature vapor-phase directed assembly process.<sup>69</sup> NIL proceeds by spin coating a 400 nm thick layer of a thermal resist onto the substrate after which it is embossed with a 1 cm<sup>2</sup> Si stamp whose surface is patterned with a hexagonal array of cylinders (240 nm diameter, 350 nm length, 600 nm pitch). Once the stamp is removed, a reactive ion etching (RIE) treatment is used to thin the patterned resist until the sub-

strate is exposed at the bottom of each cylindrical feature. Layers of Sb (12 nm) and Au (2.5 nm) are sequentially deposited onto the resist followed by a liftoff procedure that leaves an array of Au/Sb disks on the substrate. The arrays are then subjected to a heating regimen that sees them twice heated to 1010 °C in an Ar gas flow, a procedure that leaves single crystal Au seeds lined with stacking faults along their [111]-axis. The Sb, which is lost through sublimation and evaporation, is crucial in that it facilitates the assembly of Au atop each Sb disk into a single nanostructure.<sup>62</sup> The room temperature Au nanoplate synthesis proceeds by placing the seed array in a 10 mL growth solution of PVP (0.625 mL, 0.5 mM), HAuCl<sub>4</sub> (0.8 mL, 10 mM), methanol (2 mL), and DI water (6.575 mL), after which it is exposed to a broadband light source (Dolan Jenner Fiber Lite MI-150 with a B436-M fiber optic cable) for 4 h.

### 5.3 Pt@Ag core-shell synthesis

The Pt cores were formed using a high-temperature vapor-phase assembly process. It begins with the sequential deposition of thin layers of Sb (18 nm), Bi (5 nm), and Pt (7 nm) onto a [100]-oriented LSAT substrate. The sample is exposed to a heating regimen in an Ar gas flow (60 sccm) that sees them twice heated to 1100 °C in 70 min, held there for 25 min, and cooled to room temperature in 2.5 h. The procedure leaves [100]-oriented single-crystal Pt structures with random size and placement on the substrate surface. Most of the Sb and Bi are lost to the vapor phase through sublimation or evaporation where any residual quantities left on the surface are removed in a 10 s *aqua regia* etch. The low-temperature liquid-phase synthesis of Ag nanocube shells is carried out using a procedure described in detail elsewhere.<sup>55</sup> The synthesis proceeds by placing the substrate-immobilized Pt cores in a 95 °C aqueous solution of AgNO<sub>3</sub> (3 mL, 1 mM), trisodium citrate (1 mL, 10 mM), and HNO<sub>3</sub> (1 mL, 0.5 mM) for 4 min.

### 5.4 Instrumentation and characterization

SEM images and the associated EDS elemental maps and line scans were obtained using a Magellan 400 FEI field emission scanning electron microscope. TEM images and the associated SAED patterns were obtained using an FEI Titan 80–300 transmission electron microscope. TEM cross sections were prepared using a Helios Nano Lab 600 system equipped with a focused ion beam (FIB).

## Conflicts of interest

There are no conflicts to declare.

## Acknowledgements

This work is supported by a National Science Foundation Award (CMMI-1911991) to SN. It has benefitted from the facilities available through the Notre Dame Integrated Imaging

Facility (NDIIF). The authors are grateful to and acknowledge the expertise of Tatyana Orlova in the preparation of the TEM cross sections.

## Notes and references

- 1 C. Tan, J. Chen, X. J. Wu and H. Zhang, *Nat. Rev. Mater.*, 2018, **3**, 17089.
- 2 J. Liu and J. Zhang, *Chem. Rev.*, 2020, **120**, 2123–2170.
- 3 J. Zhao, B. Chen and F. Wang, *Adv. Mater.*, 2020, **32**, 2004142.
- 4 K. D. Gilroy, X. Yang, S. Xie, M. Zhao, D. Qin and Y. Xia, *Adv. Mater.*, 2018, **30**, 1706312.
- 5 M. Ha, J.-H. Kim, M. You, Q. Li, C. Fan and J.-M. Nam, *Chem. Rev.*, 2019, **119**, 12208–12278.
- 6 S. E. Habas, H. Lee, V. Radmilovic, G. A. Somorjai and P. Yang, *Nat. Mater.*, 2007, **6**, 692–697.
- 7 K. D. Gilroy, A. Ruditskiy, H.-C. Peng, D. Qin and Y. Xia, *Chem. Rev.*, 2016, **116**, 10414–10472.
- 8 M. R. Langille, J. Zhang, M. L. Personick, S. Li and C. A. Mirkin, *Science*, 2012, **337**, 954–957.
- 9 Y. Zheng, M. Luo, J. Tao, H. C. Peng, D. Wan, Y. Zhu and Y. Xia, *J. Phys. Chem. B*, 2014, **118**, 14132–14139.
- 10 M. Jin, H. Zhang, J. Wang, X. Zhong, N. Lu, Z. Li, Z. Xie, M. J. Kim and Y. Xia, *ACS Nano*, 2012, **6**, 2566–2573.
- 11 M. R. Kunz, S. M. McClain, D. P. Chen, K. M. Koczur, R. G. Weiner and S. Skrabalak, *Nanoscale*, 2017, **9**, 7570–7576.
- 12 C. F. Hsia, M. Madasu and M. H. Huang, *Chem. Mater.*, 2016, **28**, 3073–3079.
- 13 M. Tsuji, D. Yamaguchi, M. Matsunaga and M. J. Alam, *Cryst. Growth Des.*, 2010, **10**, 5129–5135.
- 14 B. T. Sneed, A. P. Young and C.-K. Tsung, *Nanoscale*, 2015, **7**, 12248–12265.
- 15 Y. Shi, Z. Lyu, M. Zhao, R. Chen, Q. N. Nguyen and Y. Xia, *Chem. Rev.*, 2021, **121**, 649–735.
- 16 X. Li, Z. Kou and J. Wang, *Small Methods*, 2021, **5**, 2001010.
- 17 B. Wu and N. Zheng, *Nano Today*, 2013, **8**, 168–197.
- 18 L. Laskar and S. E. Skrabalak, *J. Mater. Chem. A*, 2016, **4**, 6911–6918.
- 19 M. Gong, X. Jin, R. Sakidja and S. Ren, *Nano Lett.*, 2015, **15**, 8347–8353.
- 20 E. Lottini, A. López-Ortega, G. Bertoni, S. Turner, M. Meledina, G. Van Tendeloo, C. de Julián Fernández and C. Sangregorio, *Chem. Mater.*, 2016, **28**, 4214–4222.
- 21 Y. Chai, F. Feng, Q. Li, C. Yu, X. Feng, P. Lu, X. Yu, M. Ge, X. Wang and L. Yao, *J. Am. Chem. Soc.*, 2019, **141**, 3366–3370.
- 22 M. Jiang, B. Lim, J. Tao, P. H. C. Camargo, C. Ma, Y. Zhu and Y. Xia, *Nanoscale*, 2010, **2**, 2406–2411.
- 23 F.-R. Fan, D.-Y. Liu, Y.-F. Wu, S. Duan, Z.-X. Xie, Z.-Y. Jiang and Z.-Q. Tian, *J. Am. Chem. Soc.*, 2008, **130**, 6949–6951.
- 24 Y. Ma, W. Li, E. Cho, Z. Li, T. Yu, J. Zeng, Z. Xie and Y. Xia, *ACS Nano*, 2010, **4**, 6725–6734.
- 25 S. G. Kwon, G. Krylova, P. J. Phillips, R. F. Klie, S. Chattopadhyay, T. Shibata, E. E. Bunel, Y. Liu,

- V. B. Prakapenka, B. Lee and E. V. Shevchenko, *Nat. Mater.*, 2015, **14**, 215–223.
- 26 X. Xie, M. A. van Huis and A. van Blaaderen, *Nanoscale*, 2021, **13**, 2902–2913.
- 27 G. Liu, C. Zhang, J. Wu and C. A. Mirkin, *ACS Nano*, 2015, **9**, 12137–12145.
- 28 Z. Fan and H. Zhang, *Acc. Chem. Res.*, 2016, **49**, 2841–2850.
- 29 H. Ye, Q. Wang, M. Catalano, N. Lu, J. Vermeylen, M. Kim, Y. Liu, Y. Sun and X. Xia, *Nano Lett.*, 2016, **16**, 2812–2817.
- 30 M. Zhao and Y. Xia, *Nat. Rev. Mater.*, 2020, **5**, 440–459.
- 31 C. A. García-Negrete, B. R. Knappett, F. P. Schmidt, T. C. Rojas, A. E. H. Wheatley, F. Hofer and A. Fernández, *RSC Adv.*, 2015, **5**, 55262–55268.
- 32 X. Wang, S.-I. Choi, L. T. Roling, M. Luo, C. Ma, L. Zhang, M. Chi, J. Liu, Z. Xie, J. A. Herron, M. Mavrikakis and Y. Xia, *Nat. Commun.*, 2015, **6**, 7594.
- 33 C. Gao, Z. Lu, Y. Liu, Q. Zhang, M. Chi, Q. Cheng and Y. Yin, *Angew. Chem.*, 2012, **124**, 5727–5633.
- 34 Y. Yang, J. Liu, Z. Fu and D. Qin, *J. Am. Chem. Soc.*, 2014, **136**, 8153–8156.
- 35 H. Liu, T. Liu, L. Zhang, L. Han, C. Gao and Y. Yin, *Adv. Funct. Mater.*, 2015, **25**, 5435–5443.
- 36 Z. Wang, Z. Chen, H. Zhang, Z. Zhang, H. Wu, M. Jin, C. Wu, D. Yang and Y. Yin, *ACS Nano*, 2015, **9**, 3307–3313.
- 37 H. Agrawal, B. K. Patra, T. Altantzis, A. de Backer and E. C. Garnett, *ACS Appl. Mater. Interfaces*, 2020, **12**, 8788–8794.
- 38 C.-H. Kuo, L. K. Lamontagne, C. N. Brodsky, L.-Y. Chou, J. Zhuang, B. T. Sneed, M. K. Sheehan and C.-K. Tsung, *ChemSusChem*, 2013, **6**, 1993–2000.
- 39 H. L. Xin, S. Alayoglu, R. Tao, A. Genc, C.-M. Wang, L. Kovarik, E. A. Stach, L.-W. Wang, M. Salmeron, G. A. Somorjai and H. Zheng, *Nano Lett.*, 2014, **14**, 3203–3207.
- 40 B. T. Sneed, C. N. Brodsky, C.-H. Kuo, L. K. Lamontagne, Y. Jiang, Y. Wang, F. Tao, W. Huang and C.-K. Tsung, *J. Am. Chem. Soc.*, 2013, **135**, 14691–14700.
- 41 H. Zhang, C. Kinnear and P. Mulvaney, *Adv. Mater.*, 2020, **32**, 1904551.
- 42 R. D. Neal, R. A. Hughes, A. S. Preston, S. Golze, T. B. Demille and S. Neretina, *J. Mater. Chem. C*, 2021, **9**, 12974–13012.
- 43 R. A. Hughes, E. Menumerov and S. Neretina, *Nanotechnology*, 2017, **28**, 282002.
- 44 H. Zhang, Y. Liu, M. F. S. Shahidan, C. Kinnear, F. Maasoumi, J. Cadusch, E. M. Akinoglu, T. D. James, A. Widmer-Cooper, A. Roberts and P. Mulvaney, *Adv. Funct. Mater.*, 2021, **31**, 2006753.
- 45 Y. Yoo, Y. S.-i. Kim, J. Kim and B. Kim, *Nanoscale*, 2020, **12**, 6537–6544.
- 46 Y. Yoo, S. I. Kim, S. Han, H. Lee, J. Kim, H. S. Kim, J. P. Ahn, T. Kang, J. Choo and B. Kim, *Nanoscale*, 2019, **11**, 17436–17443.
- 47 K. D. Gilroy, A. Sundar, M. Hajfathalian, A. Yaghoubzade, T. Tan, D. Sil, E. Borguet, R. A. Hughes and S. Neretina, *Nanoscale*, 2015, **7**, 6827–6835.
- 48 M. S. J. Marshall and M. R. Castell, *Chem. Soc. Rev.*, 2014, **43**, 2226–2239.
- 49 A. Altberg, G. Atiya, V. Mikhelashvili, G. Eisenstein and W. D. Kaplan, *J. Mater. Sci.*, 2014, **49**, 3917–3927.
- 50 F. Silly and M. R. Castell, *Phys. Rev. Lett.*, 2005, **94**, 046103.
- 51 T. Majdi, G. Zhu, J. Carvalho, V. Jarvis, K. Meinander, J. F. Britten, G. Botton and J. S. Preston, *Appl. Phys. Lett.*, 2015, **107**, 241601.
- 52 S. Neretina, R. A. Hughes, K. D. Gilroy and M. Hajfathalian, *Acc. Chem. Res.*, 2016, **49**, 2243–2250.
- 53 A. S. Preston, R. A. Hughes, T. B. Demille, V. M. Rey Davila and S. Neretina, *Acta Mater.*, 2019, **165**, 15–25.
- 54 S. D. Golze, R. A. Hughes, S. Rouvimov, R. D. Neal, T. B. Demille and S. Neretina, *Nano Lett.*, 2019, **19**, 5653–5660.
- 55 M. Hajfathalian, K. D. Gilroy, R. A. Hughes and S. Neretina, *Small*, 2016, **12**, 3444–3452.
- 56 K. D. Gilroy, R. A. Hughes and S. Neretina, *J. Am. Chem. Soc.*, 2014, **136**, 15337–15345.
- 57 T. B. Demille, R. D. Neal, A. S. Preston, Z. Liang, A. G. Oliver, R. A. Hughes and S. Neretina, *Nano Res.*, 2022, **15**, 296–303.
- 58 Y. Chen, Z. Fan, Z. Zhang, W. Niu, C. Li, N. Yang, B. Chen and H. Zhang, *Chem. Rev.*, 2018, **118**, 6409–6455.
- 59 J. E. Millstone, S. J. Hurst, G. S. Métraux, J. I. Cutler and C. A. Mirkin, *Small*, 2009, **5**, 646–664.
- 60 P. J. Eng, T. P. Trainor, G. E. Brown Jr., G. A. Waychunas, M. Newville, S. R. Sutton and M. L. Rivers, *Science*, 2000, **288**, 1029–1033.
- 61 C. V. Thompson, *Annu. Rev. Mater. Res.*, 2012, **42**, 399–434.
- 62 P. Farzinpour, A. Sundar, K. D. Gilroy, Z. E. Eskin, R. A. Hughes and S. Neretina, *Nanoscale*, 2013, **5**, 1929–1938.
- 63 M. Wang, W. Wang, Z. Li, X. Du, X. Feng, H. Xu, W. Zhao and J. Ma, *RSC Adv.*, 2016, **6**, 4867–4871.
- 64 W. Wang, H. Yang and G. Li, *CrystEngComm*, 2013, **15**, 2669–2674.
- 65 H. Agrawal and E. C. Garnett, *ACS Nano*, 2020, **14**, 11009–11016.
- 66 W. Zhou, Z. Liu, Z. Huang, H. Lin, D. Samanta, Q. Y. Lin, K. Aydin and C. A. Mirkin, *Proc. Natl. Acad. Sci. U. S. A.*, 2020, **117**, 21052–21057.
- 67 M. Juodėnas, T. Tamulevičius, J. Henzie, D. Erts and S. Tamulevičius, *ACS Nano*, 2019, **13**, 9038–9047.
- 68 K. D. Gilroy, J. Puibasset, M. Vara and Y. Xia, *Angew. Chem., Int. Ed.*, 2017, **56**, 8647–8651.
- 69 E. Menumerov, S. D. Golze, R. A. Hughes and S. Neretina, *Nanoscale*, 2018, **10**, 18186–18194.